

Three-Dimensional Reconstruction of Weak-Lensing Mass Maps with a Sparsity Prior. II. Weighing Triaxial Cluster Halos

SHOUZHUO YANG,^{1,2} XIANGCHONG LI,^{3,4} AND NAOKI YOSHIDA^{4,5,6}

¹*Physics and Astronomy Department, Swarthmore College, Swarthmore, PA 19081*

²*Institute of High Energy Physics, Chinese Academy of Sciences, Beijing 100049, China*

³*Department of Physics, McWilliams Center for Cosmology, Carnegie Mellon University, Pittsburgh, PA 15213, USA*

⁴*Kavli Institute for the Physics and Mathematics of the Universe (WPI), University of Tokyo, Chiba 277-8583, Japan*

⁵*Department of Physics, University of Tokyo, Tokyo 113-0033, Japan*

⁶*Institute for Physics of Intelligence, University of Tokyo, Tokyo 113-0033, Japan*

ABSTRACT

Continuing work presented in Li et al. (2021), we performed a series of tests to our high-resolution three-dimensional mass map reconstruction algorithm SPLINV. We test the mass reconstruction accuracy against realistic mock catalogs generated using shear field produced by triaxial halos with the inner density profile of $\rho \propto r^{-1}$ and of $\rho \propto r^{-1.5}$. The galaxy shape noise is modeled based on the Year-1 Subaru Hyper Suprime-Cam (HSC) Survey. After reviewing mathematical details of our algorithm and dark matter halo models, we determine an optimal value of the coefficient of the adaptive LASSO regression penalty term for single halo reconstruction. We successfully measure halo masses for massive triaxial halos; the mass determination accuracy is 5 percent for halos with $M = 10^{14.6} M_{\odot}$ at $0.0625 \leq z \leq 0.2425$, and 5 percent for those with $10^{14.8} M_{\odot}$ at $0.0625 \leq z \leq 0.4675$, and 20 percent for $M = 10^{15.0} M_{\odot}$ and $M = 10^{15.2} M_{\odot}$ in the redshift range $0.0625 \leq z \leq 0.4675$. The redshift estimate accuracy is consistently below $\Delta z/z \leq 0.05$ for the above halo masses in the range $0.1525 \leq z \leq 0.4675$. We also demonstrate that the orientation of triaxial halos and systematic error in our halo model do not affect reconstruction result significantly. Finally, we present results from reconstruction of mass distribution using shear catalogs produced by multiple halos, to show SPLINV's capability using realistic shear maps from ongoing and future galaxy surveys.

Keywords: gravitational lensing: weak — galaxies: clusters: general

1. INTRODUCTION

Galaxy clusters are the heaviest gravitationally bound objects in the Universe. The redshift evolution of the abundance of galaxy clusters is sensitive to the growth rate of cosmic large-scale structures and the expansion history of the Universe. By reconstructing the number of dark matter halos at certain redshift with certain mass and comparing with halo mass function models (e.g. Tinker et al. 2010; Despali et al. 2016), one can constrain the underlying cosmological parameters including σ_8 and Ω_m . Cluster cosmology will be one of the main focuses of upcoming galaxy surveys including *Euclid* and Rubin LSST (e.g., see Laureijs et al. 2011 and Ivezić et al. 2019).

Gravitational lensing refers to the distortion of light from background galaxies due to foreground gravitational potentials. Neglecting the *B*-mode in lensing distortion (which is three orders of magnitudes smaller than *E*-mode, see Krause & Hirata 2010), this effect is usually described by 3 parameters, a spin-0 convergence κ and two components of spin-2 shear $\gamma = \gamma_1 + i\gamma_2$, where convergence changes apparent galaxy sizes, and shear anisotropically distorts galaxy shapes. By measuring the coherent anisotropy in galaxy shapes, one can infer the local shear statistically.

Due to the ubiquitousness of this signal, one can measure it from every detected galaxy at different positions and obtain a map of shear field (Li & Mandelbaum 2022). Then the convergence map can be reconstructed using the shear map (Kaiser & Squires 1993). This convergence map is also known as two-dimensional (2-D) lensing mass map since it is the integrated foreground

mass map along the line-of-sight (weighted by lensing kernel).

There are extensive studies on 2-D mass map reconstructed from weak gravitational lensing shear measurement, which focus on directly detecting galaxy clusters from weak lensing mass map without modeling the relation between optical observables and dark matter halo mass (Miyazaki et al. 2018; Hamana et al. 2020; Oguri et al. 2021). These studies detect clusters by finding peaks in the reconstructed 2-D mass map. However, 2-D lensing mass map does not provide redshift and mass information of galaxy clusters. Therefore, we cannot use a 2-D mass map to directly study the *redshift evolution* of halo mass function.

This paper focuses on detecting and weighing galaxy clusters from three-dimensional (3-D) mass map reconstructed from weak lensing shear measurements using the algorithm proposed by Li et al. (2021). The sparsity regularization — adaptive LASSO (Zou 2006) — utilized by our reconstruction should solve smearing problem of the reconstructed structures along the line of sight (Massey et al. 2007; Hu & Keeton 2002). We model the 3-D mass map as a sum of basis “atoms” in comoving coordinates as a given 3D density field. The basis “atoms” are constructed with NFW (Navarro et al. 1997) or cuspy NFW (Jing & Suto 2002) halos, which differs from other reconstruction schemes as GLIMPSE (Leonard et al. 2014) that our basis can accounted for the angular scale difference at different lens redshifts and is better suited to model clumpy mass distribution.

By numerically calculating the shear field produced by NFW and cuspy NFW halos and adding realistic noises from Hyper Supreme Cam (HSC) first-year survey (Mandelbaum et al. 2017), we attempt to reconstruct the underlying halo mass using “atoms” with density profiles described by Oguri et al. (2003).

This paper is organized as follows: In Section 2, we introduce our algorithm for 3-D mass map reconstruction. In Section 3, we study the cluster detection and cluster mass, redshift estimation from 3-D mass map using one-halo simulations with different triaxial profiles. In Section 4, we study the performance of 3-D mass map reconstruction using two-halos simulations. In Section 5, we summarize and discuss the future application of the method to weak lensing imaging surveys.

In this paper, we adopt the Λ CDM cosmology of the Planck 2018 observation of the cosmic microwave background (CMB) with $H_0 = 67.4 \text{ km s}^{-1} \text{ Mpc}^{-1}$, $\Omega_m = 0.315$, $\Omega_\Lambda = 0.685$, $\sigma_8 = 0.811$, $n_s = 0.965$ and $N_{\text{eff}} = 2.99$ (Planck Collaboration et al. 2020).

2. 3D MASS MAP RECONSTRUCTION

In this section, we review the 3-D mass map reconstruction algorithm introduced in Li et al. (2021).

2.1. Forward modelling

Under the usual Born approximation (Petri et al. 2017), the weak lensing shear field, γ , observed from background galaxy images is related to the foreground density contrast field $\delta_\theta = \rho_\theta / \bar{\rho}_\theta - 1$ through a linear transform:

$$\gamma_\theta = \sum_{\theta'} T_{\theta\theta'} \delta_{\theta'} + \epsilon_\theta, \quad (1)$$

where ϵ_θ is the error in shear measurement due to the random galaxy shapes (intrinsic shape noise) and the sky variance (photon noise). Here γ_θ , δ_θ and ϵ_θ are functions of θ , and $T_{\theta\theta'}$ is a linear mapping operator from density contrast field to shear field.

In order to reconstruct high-resolution mass maps with high signal-to-noise ratio (SNR), we incorporate prior information on the density contrast field into the reconstruction by modeling the density field as a sum of basis atoms in a “dictionary”:

$$\delta_\theta = \sum_{\theta'} \Phi_{\theta\theta'} x_{\theta'}, \quad (2)$$

where $\Phi_{\theta\theta'}$ is the matrix transforming from the projection coefficient vector x_θ to the density contrast field δ_θ . Note that a dictionary may contain multiple “frames”, used to contain halos with different density profiles. The column vectors of $\Phi_{\theta\theta'}$ are the basis “atoms” of the model dictionary.

We define the forward transforming matrix $A_{\theta\theta'} = \sum_{\theta''} T_{\theta\theta''} \Phi_{\theta''\theta'}$. With Equations (1) and (2), and write the transform from the coefficient vector x to the observed lensing shear field as

$$\gamma_\theta = \sum_{\theta'} A_{\theta\theta'} x_{\theta'} + \epsilon_\theta. \quad (3)$$

To simplify the equations in the following, we use Einstein notation:

$$\begin{aligned} A_{\theta\theta'} x_{\theta'} &= \sum_{\theta''} A_{\theta\theta''} x_{\theta''} \\ T_{\theta\theta''} \Phi_{\theta''\theta'} &= \sum_{\theta'''} T_{\theta\theta'''} \Phi_{\theta'''\theta'}. \end{aligned} \quad (4)$$

2.2. Sparsity regularization

To obtain a sparse reconstruction of mass map, we use the l^1 norm of the projection coefficient vector to regularize the modeling. The estimator is defined as

$$\hat{x}_\theta^{\text{LASSO}} = \arg \min_{x'_\theta} \left\{ \frac{1}{2} \sum_{\theta} \|(\gamma_\theta - A_{\theta\theta'} x_{\theta'})\|_2^2 + \lambda \|x_{\theta'}\|_1 \right\}, \quad (5)$$

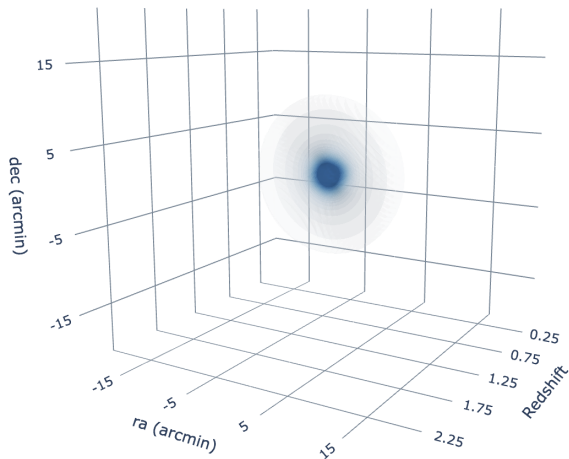


Figure 1. A sample reconstruction illustration of an isotropic halo at $z = 1.25$ with mass $M = 10^{14.6} M_{\odot}$.

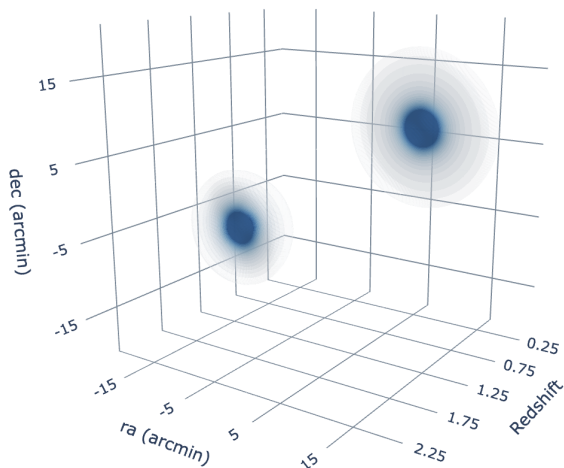


Figure 2. A sample reconstruction of underlying κ map of a 2-halo simulation using two isotropic halos at $z = 2.25$ with $M = 10^{14.8} M_{\odot}$ and $z = 1.25$ with $M = 10^{14.6} M_{\odot}$.

where $\|\cdot\|_1$ and $\|\cdot\|_2$ refer to the l^1 norm and l^2 norm, respectively, and λ is the penalty parameter for the LASSO estimation. The l^2 norm is calculated with the inverse of covariance matrix of the shape noise in the shear measurement: $C_{\theta\theta'} = \langle \epsilon_{\theta} \epsilon_{\theta'} \rangle$. As we do not smooth the observed shear map across pixels, $C_{\theta\theta'}$ and its inverse are approximately diagonal.

The LASSO algorithm searches and selects the parameters that are relevant to the measurements, and simultaneously estimates the values of the selected parameters. It has been shown by Zou (2006) that when the column vectors of the forward transform matrix \mathbf{A}'

are highly correlated, the algorithm cannot select the relevant atoms from the dictionary consistently. In addition, the estimated parameters are often biased owing to the shrinkage in the LASSO regression. We note that, for the density map reconstruction problem here, the column vectors are highly correlated even in the absence of photo- z uncertainties since the lensing kernels for lenses at different redshifts overlap significantly (Li et al. 2021). Therefore, the LASSO algorithm cannot precisely determine the consistent mass distribution in redshift, and the reconstructed map suffers from smearing in the line of sight direction even in the absence of noises.

To overcome the problems, (Li et al. 2021) adopts the adaptive LASSO algorithm proposed in Zou (2006) proposes, which uses adaptive weights to penalize different projection coefficients in the l^1 penalty. The adaptive LASSO algorithm performs a two-step process. In the first step, the standard (nonadaptive) LASSO is used to estimate the parameters. We denote the preliminary estimation as \hat{x}'_{LASSO} . In the second step, the preliminary estimate is used to calculate the non-negative weight vector for penalization as

$$\hat{w}_{\theta} = \frac{1}{|\hat{x}'_{\text{LASSO}}|_{\theta}^{\tau}}, \quad (6)$$

where we set the hyperparameter τ to 2 (Li et al. 2021). The adaptive LASSO estimator is then given by

$$\hat{x}_{\theta} = \arg \min_{x'_{\theta}} \left\{ \frac{1}{2} \Sigma \|(\gamma_{\theta} - A_{\theta\theta'} x_{\theta'})\|_2^2 + \lambda_{\text{ada}} \|\hat{w}_{\theta'} \circ x_{\theta'}\|_1 \right\}, \quad (7)$$

where “ \circ ” refers to the element-wise product. λ_{ada} is the penalty parameter for the adaptive LASSO, which does not need to be the same as the penalty parameter for the preliminary LASSO estimation λ . The adaptive weights enhance the shrinkage in the soft thresholding for the coefficients with smaller amplitudes, whereas the weights suppress the shrinkage for the coefficients with larger amplitudes.

We show examples of reconstructed mass map on halo simulations with one input halo and two input halos in Figs. 1 and 2, respectively. The details for these two cases will be discussed in Sections 3 and 4, respectively.

3. ONE HALO

In this section we test the mass map reconstruction on one-halo simulations of general triaxial halos. In Section 3.1, we present the density profile and lensing effects of triaxial halos; in Section 3.2, we describe the triaxial halo simulations used to test our mass mapping algorithm; in Section 3.3 and Section 3.4, we show the results on noiseless and noisy simulations, respectively.

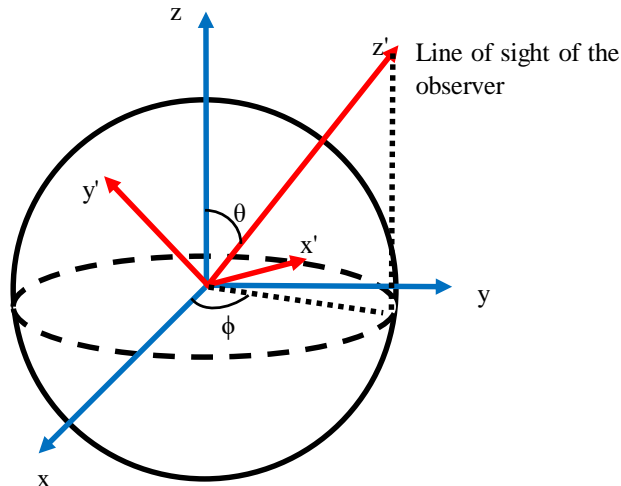


Figure 3. Orientations of the coordinate systems. The Cartesian axes (x, y, z) represent the halo principal coordinate system, while the axes (x', y', z') stand for the observer's coordinate system, with the z' -axis aligned with the line-of-sight direction. The x' -axis lies in the x - y plane. The angle θ , ϕ represents the polar angle of the line-of-sight direction in the halo's coordinate system. Adapted from Oguri et al. (2003) with permission.

3.1. Triaxial halo Simulation

3.1.1. Halo profile

Following the definition of Jing & Suto (2002), we adopt a halo density profile of

$$\rho(R) = \frac{\delta_{ce}\rho_{\text{crit}}(z)}{(R/R_0)^\alpha(1+R/R_0)^{3-\alpha}}, \quad (8)$$

where

$$R^2 \equiv c^2 \left(\frac{x^2}{a^2} + \frac{y^2}{b^2} + \frac{z^2}{c^2} \right) \quad (a \leq b \leq c). \quad (9)$$

Here, δ_{ce} is the concentration parameter of the halo. $\rho_{\text{crit}}(z)$ is the critical density of the universe at redshift z . We denote the scale radius of the triaxial halo as R_0 , and a, b and c are scaling factors that describes the shape of the halo. We set $b = c = 1$ in the rest of the analysis in this paper, for simplicity and normalization.

From equation (8), we see that the case of an isotropic halo model with $\alpha = 1$ reproduces the NFW halo profile. Various literature uphold different values of α ranging between $\alpha = 1$ and $\alpha = 1.5$ (see e.g., Navarro et al. 1997, Moore et al. 1999, Oguri et al. 2003). Therefore, we perform our subsequent analyses both for halos with $\alpha = 1$ and $\alpha = 1.5$.

Jing & Suto (2002) also define a length scale R_e such that $R_e/r_{\text{vir}} = 0.45$ (r_{vir} is the virial radius) and $\frac{R_e}{R_0} =$

c_e is the concentration parameter. The average density within an ellipsoid of R_e is

$$\Delta_e = 5\Delta_{\text{vir}}\left(\frac{c^2}{ab}\right)^{0.75}, \quad (10)$$

where, from Oguri et al. (2001a), we have

$$\Delta_{\text{vir}} = \frac{3M_{\text{vir}}}{4\pi r_{\text{vir}}\rho_{\text{crit}}} = 18\pi^2(1 + 0.4093\omega_{\text{vir}}^{0.9052}). \quad (11)$$

Assuming that $\Omega_m + \Omega_\Lambda = 1$, $\omega_{\text{vir}} = 1/\Omega_{\text{vir}} - 1$, and the density parameter Ω_{vir} at the redshift of virialization z_{vir} is (Oguri et al. 2001b)

$$\Omega_{\text{vir}} = \frac{\Omega_m(1+z_{\text{vir}})^3}{\Omega_m(1+z_{\text{vir}})^3 + (1-\Omega_m-\Omega_\Lambda)(1+z_{\text{vir}}^2) + \Omega_\Lambda}. \quad (12)$$

In this paper, we take the empirical relation between the concentration parameter ($c \equiv \frac{r_{\text{vir}}}{R_0}$), the virial mass (M_{vir}) and redshift (z) of the halo:

$$c = A \left(\frac{M_{\text{vir}}}{10^{13}M_\odot} \right)^B \left(\frac{1.47}{1+z} \right)^C \quad (13)$$

where $A = 6.02$, $B = -0.12$, $C = 0.16$, and M_\odot is the solar mass (Child et al. 2018).

3.1.2. Convergence and Shear of Triaxial Halos

To describe rotations of a triaxial halo, we introduce two coordinate systems: The (x, y, z) system is the dark matter halo's system, with its origin at the halo's center and z axis lies along the major principle axis of the halo. The (x', y', z') coordinate represent the observer's coordinate system, with its origin also set at the halo's center. We define (θ, ϕ) to be the polar coordinates of the line-of-sight direction of the observer with the halo's long axis as the z -axis. Just like Oguri et al. (2003), we note that the x' -axis lies in the x - y plane. We also define ζ such that

$$\zeta = \frac{c^2}{b^2}x'^2 + \frac{c^2}{a^2}y'^2, \quad (14)$$

where the primed coordinate (x', y') represent normalized observer's coordinate. Fig. 3 is an illustrative plot that shows the relationship between the coordinates. Then we get an expression for the lensing convergence κ as:

$$\begin{aligned} \kappa &= \frac{R_0}{\Sigma_{\text{crit}}} \int_{-\infty}^{\infty} \rho(R) dz' = \frac{R_0}{\Sigma_{\text{crit}}} \int_{-\infty}^{\infty} \frac{\rho(\sqrt{z_*'^2 + \zeta^2})}{\sqrt{f}} dz_*' \\ &\equiv \frac{b_{\text{TNGFW}}}{2} f_{\text{TNGFW}}(\zeta) \end{aligned} \quad (15)$$

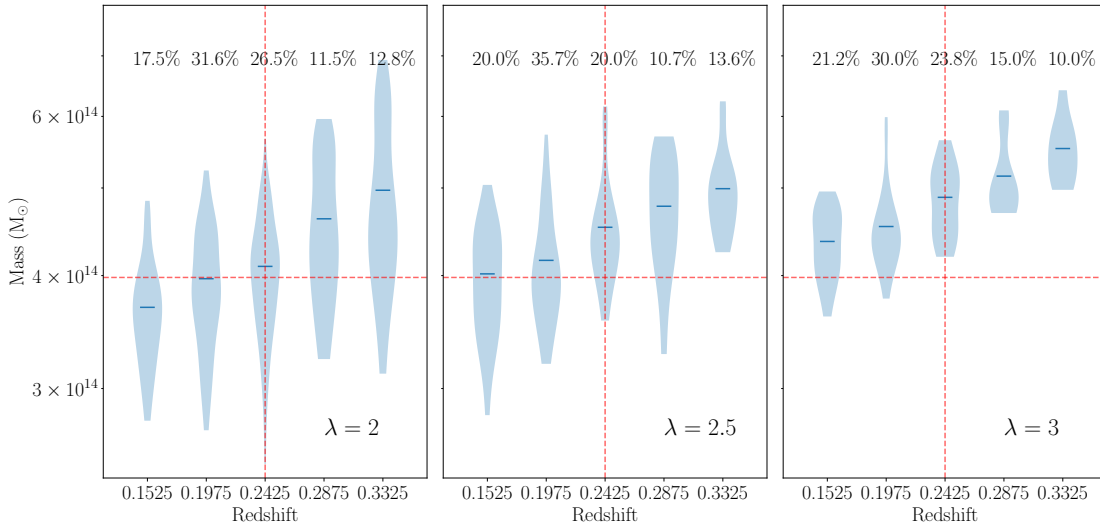


Figure 4. Detected halo number density as a function of measured redshift and measured mass with different sparsity parameters. The shaded blue area shows the number density as a function of measured mass located at each redshift. The input halo has mass $10^{14.6} M_{\odot}$. The number above each probability distribution shows the fraction of halos detected at the corresponding redshift. The detection rates are 47%, 28%, and 16% from the left to the right panel, respectively.

where

$$b_{\text{TNGW}} \equiv \frac{1}{f} \frac{4\delta_{\text{ce}} \rho_{\text{crit}}(z) R_0}{\Sigma_{\text{crit}}}, \quad (16)$$

with $f = \sin^2 \theta \left(\frac{c^2}{a^2} \cos^2 \phi + \frac{c^2}{b^2} \sin^2 \phi \right) + \cos^2 \theta$, and

$$f_{\text{TNGW}} \equiv \int_0^{\infty} \frac{1}{(\sqrt{r^2 + z^2})^{\alpha} (1 + \sqrt{r^2 + z^2})^{3-\alpha}} dz. \quad (17)$$

The subscripts, “TNGW”, corresponds to “Triaxial NFW”. Σ_{crit} is the lensing critical surface mass density defined as

$$\Sigma_{\text{crit}} \equiv \frac{c^2 D_{\text{OS}}}{4\pi G D_{\text{OL}} D_{\text{LS}}},$$

where D_{OL} , D_{OS} , and D_{LS} are the angular diameter distances from the observer to the lens plane, from the observer to the source plane, and from the lens plane to the source plane, respectively.

Once we have an expression for κ , we may follow Keeton (2001) to calculate the shear field. Note that although in $\alpha = 1$ case an analytical solution can be yield, an analytical solution does not exist for a density profile with $\alpha = 1.5$. Differing from equation (4) in Li et al. (2021), we did not adopt truncation at the viral radius to facility numerical computation of shear fields.

3.2. Simulation setup

In this subsection, we introduce our simulations used to test the mass map reconstruction algorithm and quantify biases in the halo mass and redshift estimations from the reconstructed mass map..

3.2.1. Lensing Shear

We use halos with different triaxial shapes to produce shear fields for simulation. This is represented with a wide range of ellipticity, defined as $\frac{a}{c}$ (see equation 9). However, to reduce dimensionality and computational time during the mass map reconstruction, the dictionaries are prepared with isotropic halos with $a = b = c = 1$ described in the previous section. The shear field are measured at redshift of $z = 0.05, 0.36, 0.47, 0.56, 0.69, 0.80, 0.91, 1.03, 1.22, 1.50,$ and 2.50 .

To consider variation of halo profiles as found in recent high-resolution N -body simulations (Navarro et al. 2010), we include the ability to simulate shear field produced by triaxial halos (Jing & Suto 2002) with both (i) the NFW radial profile with $\alpha = 1$ in equation (8) (Navarro et al. 1997) and (ii) the cuspy NFW radial profile with $\alpha = 1.5$ (Jing & Suto 2000).

3.2.2. Observational Noise

We account for statistical uncertainties in shape estimation from galaxy intrinsic shape noise and measurement error due to image noise, calculated using the first-year shear catalog of the HSC first-year data (Mandelbaum et al. 2017). Specifically, we utilized the formulation of Shirasaki et al. (2019), where we have

$$\epsilon^{\text{int}} = \left(\frac{e_{\text{rms}}}{\sqrt{e_{\text{rms}}^2 + \sigma_e^2}} \right) e^{\text{ran}}, \quad \epsilon^{\text{mea}} = N_1 + i N_2.$$

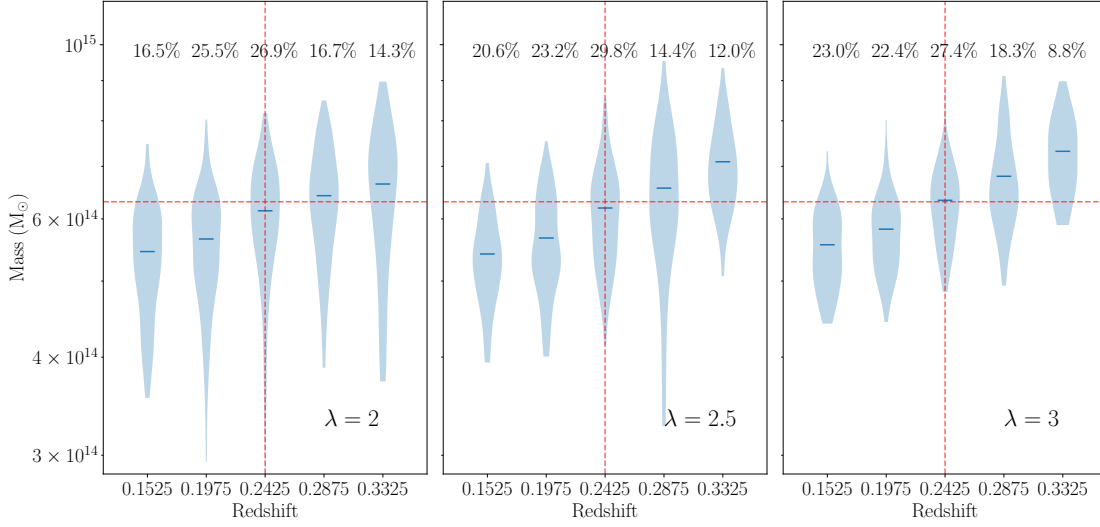


Figure 5. Similar to Fig. 4, but for halos with mass $10^{14.8} M_{\odot}$. The detection rates are 82%, 77%, and 68% from the left to the right panel, respectively.

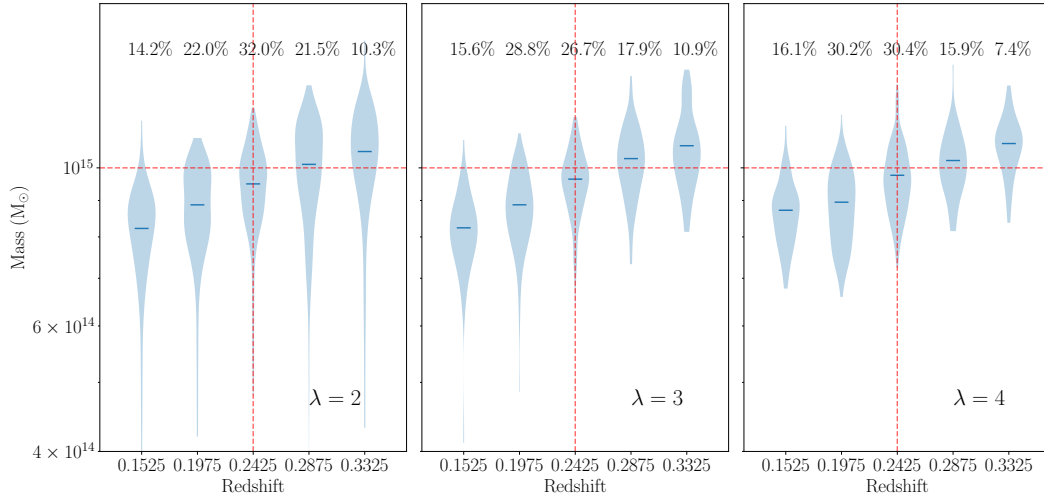


Figure 6. Similar to Fig. 4, but for halos with mass $10^{15.0} M_{\odot}$. The detection rates are 89%, 95%, and 95% from the left to the right panel, respectively.

In the above expression ϵ^{int} represents the per-component intrinsic shape error, and ϵ^{mea} represents the per-component shape measurement error. Also, $e^{\text{ran}} = e^{\text{obs}} e^{i\phi}$, where e^{obs} is the distortion of some individual galaxy and $e^{i\phi}$ serves to rotate the observed shape by some random angle ϕ . N_1 and N_2 are random numbers drawn from a Gaussian centered at 0 with a

standard deviation of σ_e . ϵ_{rms} is the root-mean-square of the intrinsic galaxy shape for each shape component. σ_e is the standard deviation of the shape measurement error due to image noise for each shape component. Note, ϵ_{rms} and σ_e are estimated from image simulations at single galaxy level using realistic galaxy image simulations (Mandelbaum et al. 2018a).

We assume that the multiplicative and additive biases in the shear catalog is fully corrected in this paper; therefore, we have an expression for the observed shear:

$$\gamma^{\text{obs}} = \frac{\epsilon}{2\mathcal{R}}, \quad (18)$$

where $\mathcal{R} = 1 - \langle \epsilon_{\text{rms}}^2 \rangle$. We can then substitute

$$\epsilon = \epsilon^{\text{ran}} + \epsilon^{\text{mea}}$$

to get a mock shear field.

For realistic noisy tests, we adopt realistic HSC-like galaxy number density ($\sim 20 \text{ arcmin}^{-2}$) (Mandelbaum et al. 2018b; Li et al. 2022) when producing shear fields in order to test the performance of our algorithm with noisy setup. However, for the noiseless tests in section 3.3, we adopt an extremely high galaxy number density (2000 arcmin^{-2}) to suppress the random noise in the sub-pixel galaxy distribution.

3.3. Results: Noiseless Case

In this section, we discuss the mass map reconstruction results for triaxial NFW ($\alpha = 1$) and cuspy NFW ($\alpha = 1.5$) halos noiseless simulations. An example of the reconstructed 3-D map is shown in Fig. 1.

- (i) Indicating the type(s) of halo(s) from which a dictionary desires to be built. This includes the density profile of the halo (in this work, we only use NFW or the cuspy NFW halo but there are more possibilities), the masses of the halos and either the concentration parameter or the scale radius of the halos. Note that a set of dictionary may contain a mixture halo models.
- (ii) To generate noiseless κ field, we prepared a set of function to calculate halo's κ field from its density profile and other properties. We sample equation (15) with 500 points per square arcmin and pixelize the map. Note, when creating the κ map, we do not smooth to introduce correlation between pixels
- (iii) Use Kaiser-Squire (Kaiser & Squires 1993) transformation to acquire the noiseless underlying shear field produced by the halo specified by the above parameters.

We first investigated the relative mass bias (defined to be the difference between true mass and the reconstructed mass over true mass) in SPLINV's estimation from noiseless shear field. We performed in total of 100 reconstructions, for halos having 10 redshift values from $z = 0.0625$ to $z = 0.4675$ and 10 ellipticity

values from $\frac{a}{c} = 1$ to $\frac{a}{c} = 0.5$. We chose $\lambda = 2$ because this value is our fiducial value for later noisy reconstruction and specific value of λ does not affect reconstruction result significantly in this noiseless reconstruction. We repeated the above procedure for three masses: $M_{\text{vir}} = 10^{14.6} M_{\odot}$, $10^{14.8} M_{\odot}$, and $10^{15.0} M_{\odot}$. We put each halo in the center of in a 48×48 pixelized grid covering $98 \text{ arcmin} \times 98 \text{ arcmin}$ of sky area. Our result shows that near-isotropic halo reconstruction gives exquisite mass estimation: for halos with $0.8 \leq \frac{a}{c} \leq 1$, mass bias is consistently around or below percent-level across $z = 0.0625$ to $z = 0.4675$. We conclude that the noiseless reconstruction at a lower redshift ($z \leq 0.2425$) only has 5% of mass bias even when the halo is highly anisotropic, while the highest mass bias at $z = 0.3325$ is less than 10%. There are some instances where SPLINV overestimates the redshift of halos with a small $\frac{a}{c}$ in high redshifts. We think this is due to the fact that a smaller $\frac{a}{c}$ values correspond to a smaller halo as it appears along the line-of-sight direction, and therefore the SPLINV will tend to approximate the field with halo with a smaller radius, corresponding to a higher redshift.

3.4. Results: Noisy Case

This is our result section on how SPLINV performs reconstructing a noisy shear field. We first analyzed how the λ value affects the reconstruction results in Sect. 3.4.1 and set a fiducial value of $\lambda = 2$. Then in Sect. 3.4.2 and Sect. 3.4.3 we show the result of mass and redshift estimation from noisy reconstructions. In 3.4.4, we study the potential model bias due to the difference between halo models in the universe and those used in our dictionary.

3.4.1. Performance with different λ

The performance of the our mass mapping algorithm may depend on the regularization parameter λ for the noisy case. We present the how SPLINV behaves differently with different λ values in this section.

To determine the sparsity parameter λ in equation (5) that optimizes reconstruction results, we perform various single halo reconstruction of shear field produced by an isotropic halo of mass $10^{14.6}$, $10^{14.8}$, and $10^{15.0}$ respectively, at an intermediate redshift ($z = 0.2425$) in the center of in a 48×48 pixelized grid covering $98 \text{ arcmin} \times 98 \text{ arcmin}$ of sky area. Examining the density plots (Figs. 4–6) for different values of λ , we find that while “the best” λ parameter potentially exists for each case, a smaller λ value tend to make SPLINV to provide a smaller mass estimation than those provided by SPLINV with a larger λ , most likely due to a smaller λ relaxes the sparsity condition as can be seen in equation (5).

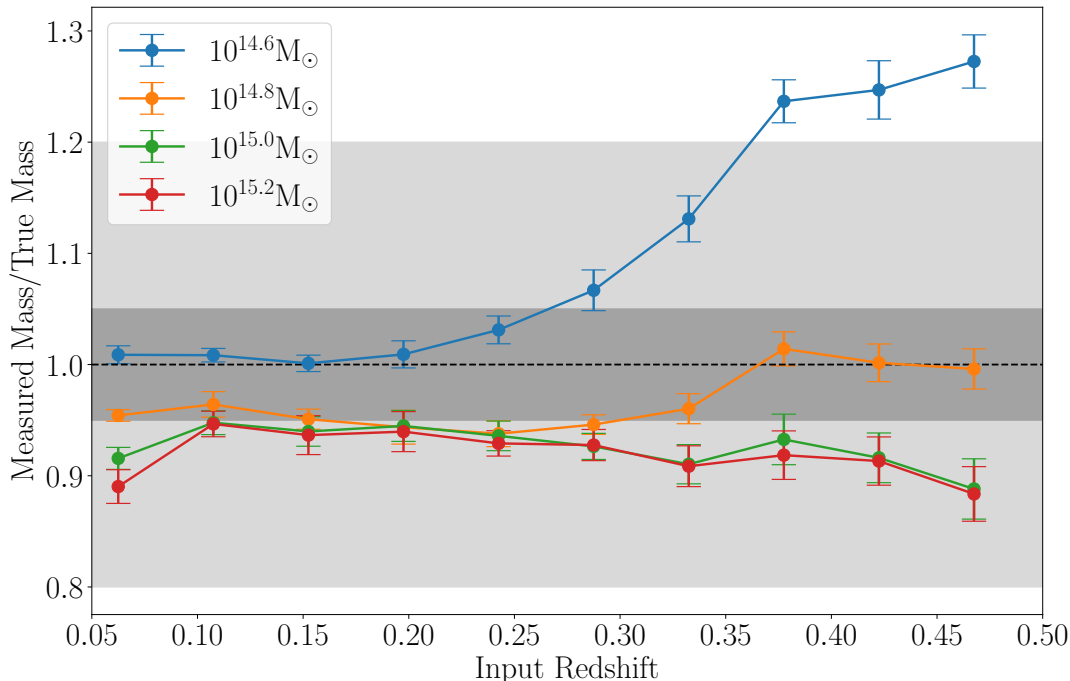


Figure 7. NFW halo ($\alpha = 1$) mass bias for $M = 10^{14.6}, 10^{14.8}, 10^{15.0},$ and $10^{15.2} M_{\odot}$. The mass maps are reconstructed with $\lambda = 2$. The darker grey area indicate a 5% bias and the lighter grey area indicate a 20% relative mass bias. The error bar indicate the standard deviation of reconstructed mass with respect to the ellipticity (a/c) over the range $[0.5, 1]$.

We conclude that a relatively higher λ should more strongly enforce the sparsity condition, while effectively making a cutoff for false detections with small masses. For this same reason, larger λ reduce the probability of detecting halos with small masses.

We find that the optimal value of λ depends on both the mass and the redshift of the halo, as reconstruction of a halo with larger SNR (higher mass and lower redshift) prefers a larger λ . From this, we conclude that we should find an optimized λ for interval targeted detection mass/redshift, and then recursively apply SPLINV to detect galaxy halo in each mass/redshift interval. For detecting halos with relatively smaller masses ($10^{14.6} M_{\odot}$), authors recommend using $\lambda = 2$ and for halos with large masses $10^{15.2} M_{\odot}$, we recommend using $\lambda = 4$. We leave the study on the optimal setup of λ using realistic ray-tracing simulations (Takahashi et al. 2017) to future works. More specifically, what our findings can be concluded as:

- (i) For simulations with small halo masses ($10^{14.6} M_{\odot} \leq M \leq 10^{14.8} M_{\odot}$), we find a $\approx 18\%$ positive mass estimation bias exists for reconstruction with $\lambda \geq 2.5$. This is possibly due to a form of Eddington Bias (e.g., see Kelly (2007)

and Eddington (1913)), where only halo's shear signal boosted by noises gets detected which are then confused with halo with a large mass.

- (ii) For halos with larger mass ($M \geq 10^{15.0} M_{\odot}$) we do not find significant mass bias with $\lambda \geq 3$ due to the high SNR of these halos.
- (iii) For halos with larger mass, SPLINV slightly underestimate halo masses with small λ ($\lambda \leq 2.5$). This is possibly because the strong signal of higher mass halos may be cause the sparsity condition of SPLINV to fail and be construed by our algorithm as caused by multiple halos.

Because we found SPLINV with $\lambda = 2$ performs well with smaller mass halos (which are more abundant in the universe) and only suffers overestimation slightly, we set $\lambda = 2$ as fiducial setup and put results with $\lambda = 4$ into Appendix (A).

3.4.2. Mass Estimation

In this section, we present reconstruction results for triaxial NFW ($\alpha = 1$) and cuspy NFW ($\alpha = 1.5$) halos.

We simulate 100 halos with 10 different shapes (from $\frac{a}{c} = 1$ to $\frac{a}{c} = 0.5$) and 10 different redshifts (from $z =$

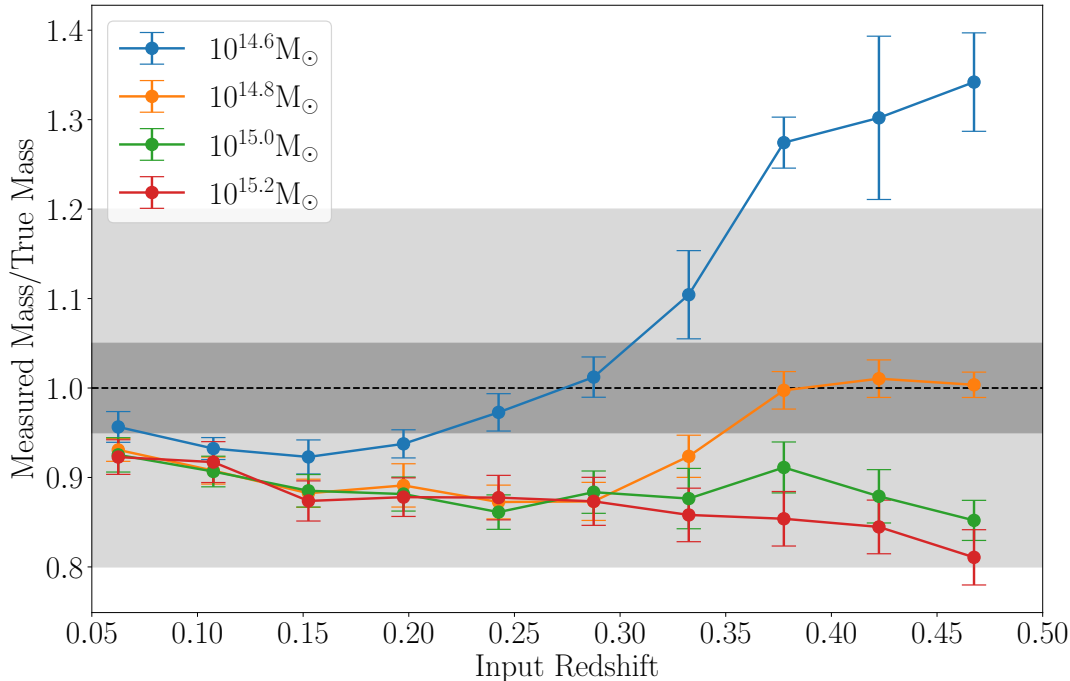


Figure 8. Cuspy NFW halo ($\alpha = 1.5$) mass bias for $M = 10^{14.6}, 10^{14.8}, 10^{15.0}$, and $10^{15.2} M_{\odot}$, respectively. The mass maps are reconstructed with $\lambda = 2$. The darker grey area indicate a 5% bias and the lighter grey area indicate a 20% relative mass bias. The error bar indicate the standard deviation of reconstructed mass with respect to the ellipticity (a/c) over the range [0.5, 1].

0.0625 to $z = 0.4675$), and for each halo, we generate 500 realizations of observational noise as described in Section 3.2.2.

In Figs. 7 and 8, we show the estimated relative mass biases for the two types of halo with ellipticity ($\frac{a}{c}$) ranging from 1 to 0.5 reconstructed with dictionary generated numerically with the same mass and concentration parameter, but with $\frac{a}{c} = 1$ (isotropic). At lower redshifts, corresponding to stronger lensing signal, the choice of $\lambda = 2$ gives halo mass estimations with error less than 10% or even better. Observing the first panel in Figs. 7 and 8, we again see the effect that, because the shear produced by the underlying halo was too small, even with $\lambda = 2$, only the halos whose shear was boosted by noise gets picked up by our algorithm, resulting in an overestimation. However, the non-monotonous pattern in the second panel of Figs. 7 and 8 indicates that one could potentially optimize the value of λ for each halo at each redshift. We also see that for reconstruction of more massive halos results in an underestimation of masses. This could be caused by the fact that a smaller λ enforces a weaker sparsity condition and SPLINV may confuse the large signal due to the massive halo as signal generated by two separate halos. Another trend we

find is that, the smaller cuspy NFW halos are generally more significantly affected by noise and hence will tend to have larger mass estimation bias.

Additionally, we find that there is a small $\frac{a}{c}$ dependence on the estimated mass bias. However, this dependence is not nearly as strong as that in the noiseless case, which tells us that we should focus on optimizing the value of λ or other detection strategies before we try to include other parameters (like the triaxiality of halo models or its rotation) that complicate our dictionary space.

3.4.3. Redshift Estimation

Here we present the results of redshift estimations from noisy reconstructions in Figs. 9 and 10. We note that the slight overestimation of redshift for halos with low redshifts in the figures is due to the discrete nature and the lower boundary of the redshift bins: there cannot be an underestimation for redshifts for these halos. Other than this, we observe that the amplitude of the relative redshift estimation bias is consistently below 5%, with no significant dependence on the shape ($\frac{a}{c}$ value) of the halo.

3.4.4. Model Bias

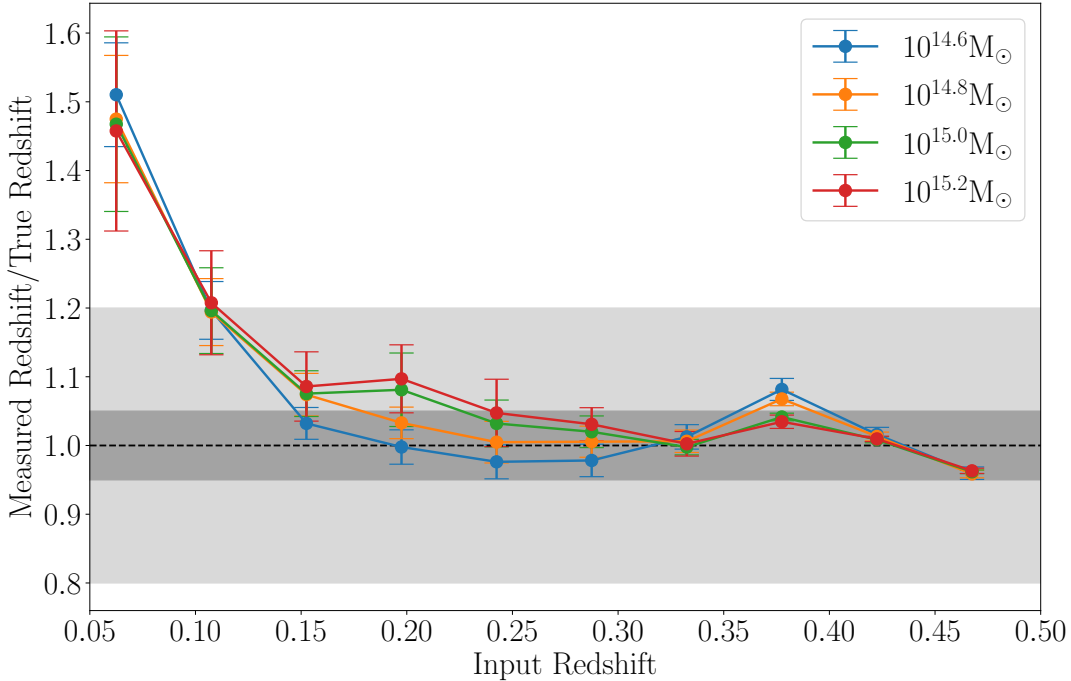


Figure 9. NFW halo ($\alpha = 1$) redshift estimation for $M = 10^{14.6}, 10^{14.8}, 10^{15.0},$ and $10^{15.2} M_{\odot}$, respectively. The mass maps are reconstructed with $\lambda = 2$. The darker grey area indicate a 5% bias and the lighter grey area indicate a 20% relative mass bias. The error bar indicate the standard deviation of reconstructed mass with respect to $\frac{m}{c}$ over the range $[0.5, 1]$.

In the previous sections, we focus on the cases where halo model used for reconstruction is the same as those used to create the shear field. In this section, we study the potential model bias due to the systematic difference between halo models in the universe and those used in our dictionary. Following the previous sections, we are using isotropic models in our model dictionary. In this section, we study the mass and redshift estimation under the condition that the dictionary used for construction does not match the underlying halo in the simulation that produces the shear field.

In Fig. 11, we show the effect of systematic error due to the models used for mass map reconstruction being different. More specifically, we show the result of estimating mass of a cuspy halo with the assumption that the underlying mass field is composed of NFW halos. Comparing Fig. 11 with Fig. 5, we find that although we used the “wrong” dictionary in Fig. 11, the reconstructed result still resembles that in Fig. 5.

Next, we study whether the just using isotropic halo models in our dictionary affect our ability to reconstruct highly anisotropic halos. Comparing Fig. 12 with the left panel of Fig. 5, we see good agreement with reconstruction using isotropic halo model and we rotate a highly anisotropic halo with $\frac{a}{c} = 0.5$ in the polar

direction for $\theta = 30^{\circ}, 60^{\circ}, 90^{\circ}$. A set of illustrative plots is shown in Fig. 13. The results from this section and the previous one indicate that, even when the true halo that constitutes the κ map of the universe may be anisotropic, one may still recover the underlying mass map using isotropic models.

4. MULTIPLE HALOS

In this section we test our algorithm under the following conditions: (i) Reconstruct mass map from noiseless shear field produced by 2 halos with different separations; (ii) Reconstructing from noisy shear field produced by multiple halos.

4.1. Noiseless Two-halo Simulations

We start this series of simulation with two isotropic NFW halo of mass $10^{14.8} M_{\odot}$ at the same redshift of $z = 0.2425$ and change the distance from 40 arcmin to 0 arcmin in a 48×48 pixelized grid covering 98 arcmin \times 98 arcmin of sky area.

Specifically, we decrease the distance between the two halos on the grid (as measured by ra and dec) by linear intervals, and perform the reconstructions until the reconstruction fails, where either the number of halo detected is wrong or the redshift estimate of either one of

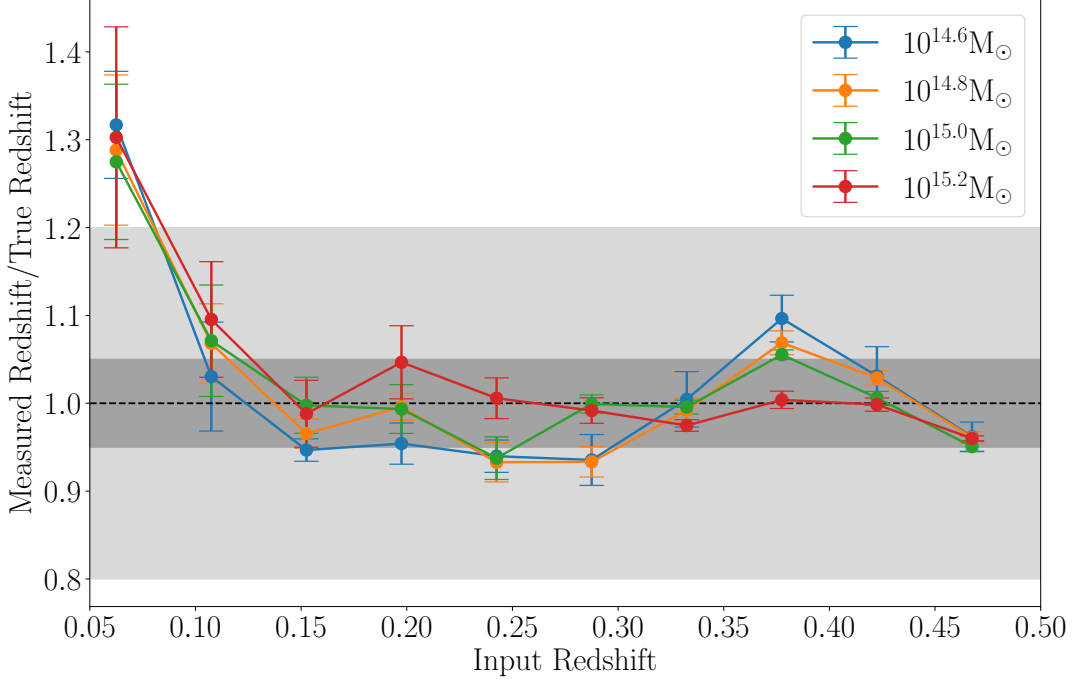


Figure 10. Cuspy NFW halo ($\alpha = 1.5$) redshift estimation for $M = 10^{14.6}, 10^{14.8}, 10^{15.0}$, and $10^{15.2}$, respectively. The mass maps are constructed with $\lambda = 2$. The darker grey area indicate a 5% bias and the lighter grey area indicate a 20% relative mass bias. The error bar indicate the standard deviation of reconstructed mass with respect to $\frac{m}{c}$ over the range $[0.5, 1]$.

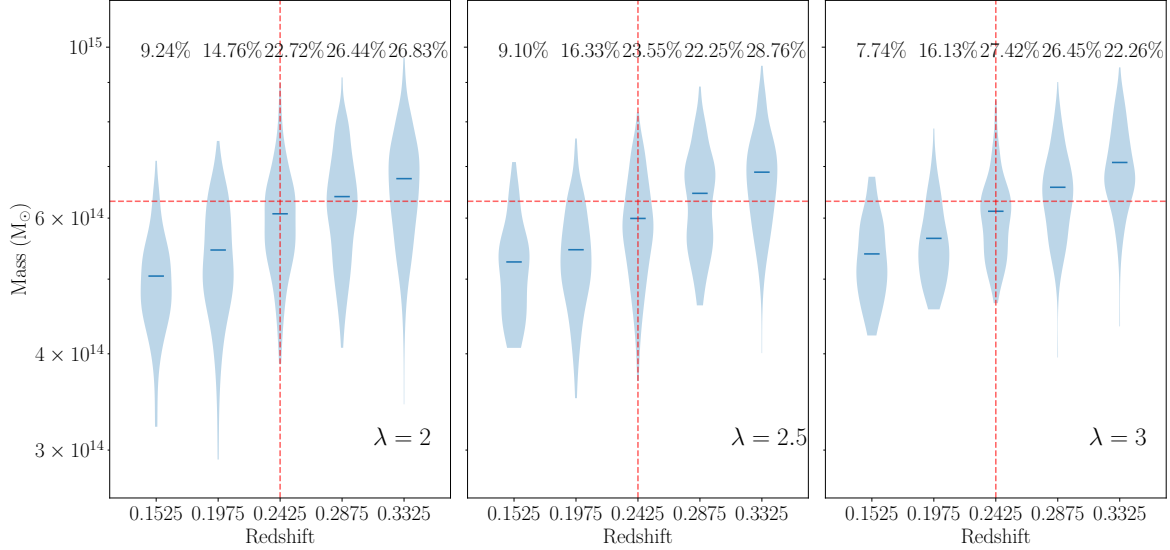


Figure 11. Detected halo number densities of cuspy NFW halo with mass $10^{14.8} M_{\odot}$ using NFW halo as dictionaries. The blue shaded area indicate the number density of detected mass that correspond to the indicated mass and redshift. The percentage above one probability distribution represents the percent of total correct estimation corresponding to the respective redshift. The true detection probabilities are 78%, 69%, and 62% for each value of λ respectively.

the halos is wrong (meaning that the redshift estimation

of the halos has to be *exact*). The other aspects of the simulation and reconstruction are identical to 3.2.

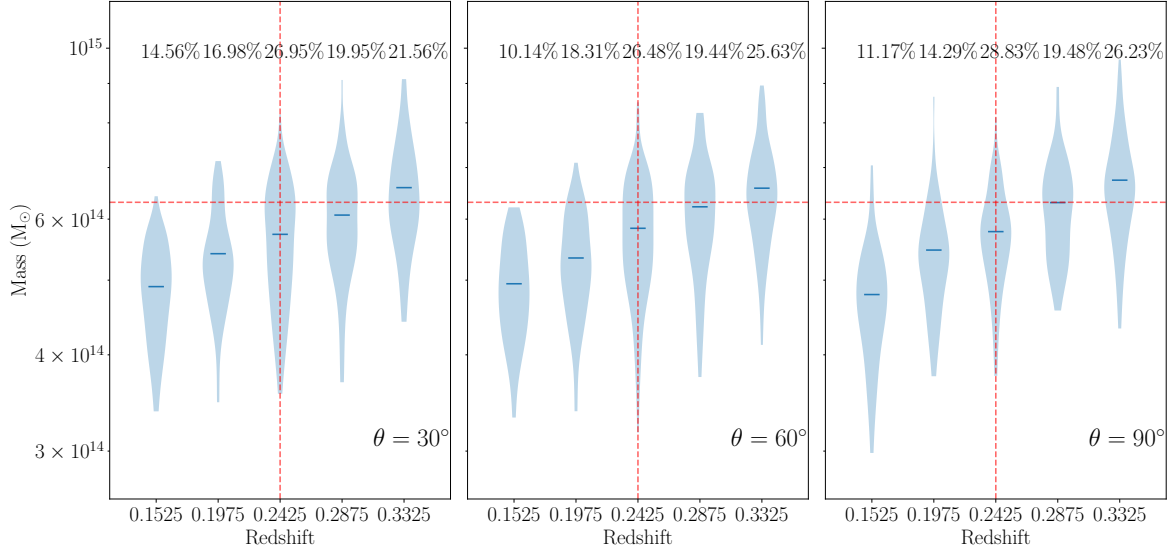


Figure 12. Detection number density plot of NFW halo with $\frac{a}{c} = 0.5$ with mass $10^{14.8} M_\odot$, but with $\theta = 30^\circ, 60^\circ, 90^\circ$. The shaded blue area indicate the number density of detected mass that correspond to the indicated mass and redshift. The percentage above one probability distribution represents the percent of total correct estimation corresponding to the respective redshift. The detection probabilities are 74%, 71%, and 77% for each value of λ respectively.

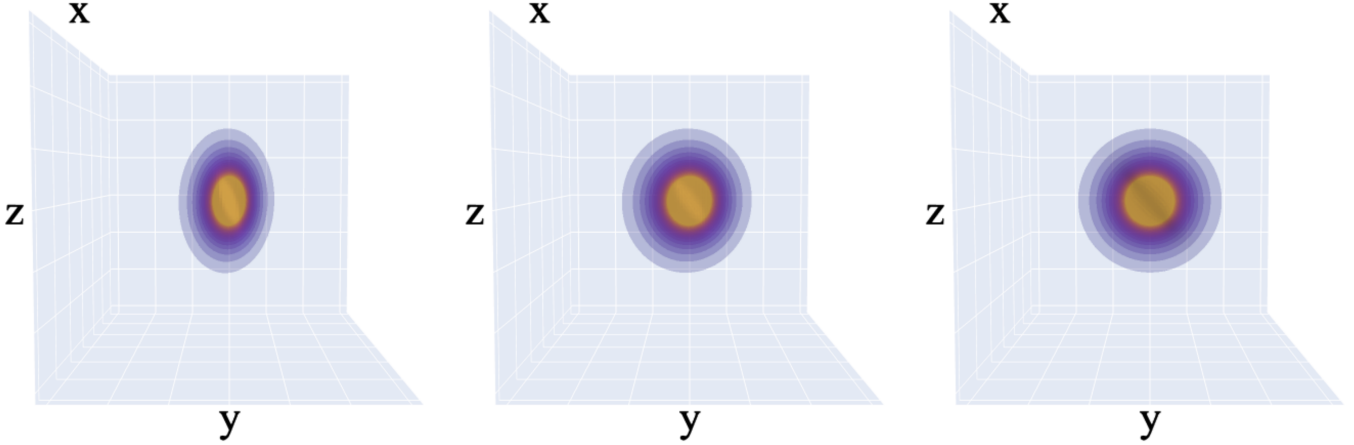


Figure 13. A set of sample plot of halo density profile with halo with $\theta = 30^\circ, 60^\circ$, and 90° , respectively.

An example of the reconstructed 3-D map is shown in Fig. 2. We observe that until the borderline of 4 arcmin, the mass estimation of the two halos are consistently below 6%. Hence, we should be concerned about significant mass bias due to halos closer or around this cutoff in noisy reconstructions, where signals of two adjacent halo combined with noise together creates a shear estimation that resembles a different halo (false detection) which affects the mass and redshift estimation of the original halo.

4.1.1. Noisy Multiple Halo Simulation

To test the performance of our algorithm in realistic multi-halo cases, we consider the following simulation set-up. We use the same parameters adopted in the previous sections but with a sky covering $256 \text{ arcmin} \times 256 \text{ arcmin}$ area, corresponding to $128 \text{ pixels} \times 128 \text{ pixels}$. The center of the stamp is set to $(ra, dec) = (0^\circ, 0^\circ)$. The three cases are:

- (i) The first halo has $M = 10^{14.8} M_\odot$ at $z = 0.1975$ with $ra = 4440''$ and $dec = 5520''$, and the sec-

ond halo has $M = 10^{14.6} M_{\odot}$ at $z = 0.2875$ with $ra = -4440''$ and $dec = -4440''$. The distance are chosen to be far enough so that, even in the noisy simulations, there is little chance that two of the halos are falsely detected as one.

- (ii) The first halo has $M = 10^{14.8} M_{\odot}$ at $z = 0.2875$ with $ra = 4440''$ and $dec = 5520''$. The second halo has $M = 10^{15.2} M_{\odot}$ at $z = 0.3775$ with $ra = -4440''$ and $dec = -4440''$. The third halo has $M = 10^{14.6} M_{\odot}$ at $z = 0.1975$ with $ra = 0''$ and $dec = 0''$. The distance are chosen to be far enough so that, even in the noisy simulations, there is little chance that two of the halos are falsely detected as one.
- (iii) Same with (ii) but we first perform a reconstruction with dictionary containing one halo with $M = 10^{15.2} M_{\odot}$ (with a higher lambda) first, and then subtract the shear field produced by a realistic reconstruction result, containing information on estimated mass and redshift.

The halo models used for the simulations and the reconstructions are both isotropic in this section.

In Fig. 14, we present result of case (i) with dictionary composed of halos with $M = 10^{14.6} M_{\odot}$ and with $M = 10^{14.8}$ with $\lambda = 2$. While the estimation for the halo with $M = 10^{14.6} M_{\odot}$ is accurate, we see an overestimation of halo mass for the halo with $M = 10^{14.8} M_{\odot}$. This is probably due to the fact that we chose a generally small λ for the halo with this mass and a SPLINV confuses the shear field produced by the $10^{14.8} M_{\odot}$ halo with that produced by the $10^{14.6} M_{\odot}$, but with a much larger mass to match the strength of shear field. The slight decrease in detection probability is probability due to increase in parameter space caused by one additional available choice of atom which causes the gradient descent algorithm harder to converge.

In Fig. 15 and Fig. 16, we show reconstruction results of the two smaller mass halo in case (ii) (a good detection on the more massive halo can always be achieved with a high value of λ). This is done in 2 ways: in the first method, we used $\lambda = 2$ and with dictionary composed of halos with $M = 10^{14.6} M_{\odot}$ and with $M = 10^{14.8} M_{\odot}$ without modifying the shear field. In the second method we first perform some detections of the larger mass halo.

Randomly select a set of mass and redshift estimation (we used $M \approx 10^{15.11} M_{\odot}$ and $z = 0.2875$ to produce the result), and then proceed with reconstruction of the remaining two halos with $\lambda = 2$ and with dictionary composed of halos with $M = 10^{14.6} M_{\odot}$ and with $M = 10^{14.8} M_{\odot}$.

We find that there is no significant difference in performance whether we subtract the shear field produced by the large halo or not. However, the underestimation in halo with $M = 10^{14.8} M_{\odot}$ and overestimation in halo with $M = 10^{14.6} M_{\odot}$ is still present. This result shows that, if we focus on detecting smaller mass halos, we may safely use dictionaries of those smaller mass halos without worrying about the shear field produced by large mass halos to interfere with our detection, keeping in mind that any anomalous large mass estimation may be caused by some large halo.

5. SUMMARY

We performed a set of systematic tests on the 3D mass map reconstruction algorithm, SPLINV, presented in Li et al. (2021). SPLINV can detect NFW and cuspy NFW halos with $M = 10^{14.6} M_{\odot}$ with less than 5% mass bias in $0.0625 \leq z \leq 0.2425$, $10^{14.8} M_{\odot}$ with less than 5% mass bias in $0.0625 \leq z \leq 0.4675$ and with less than 20% mass bias for halo with $M = 10^{15.0} M_{\odot}$ and $M = 10^{15.2} M_{\odot}$ in the redshift range $0.0625 \leq z \leq 0.4675$. The redshift bias is consistently below $5\%z$ for the above halo masses in the range for $0.1525 \leq z \leq 0.4675$. We also demonstrated that rotations of triaxial halo models and systematic error in halo modeling (e.g. we measure cuspy NFW halos with the assumption that underlying mass field of the universe is consisted of NFW halos) does not affect reconstruction result significantly. Our multiple halo reconstruction case demonstrated SPLINV's strong applicability to reconstruction to observed shear catalogs measured by for example HSC and LSST in the future.

ACKNOWLEDGEMENTS

This work is partially supported by Swarthmore College Honors Fellowship.

DATA AVAILABILITY

The code used in this paper is available from <https://github.com/mr-superonion/splinv/>.

REFERENCES

- Child, H. L., Habib, S., Heitmann, K., et al. 2018, The Astrophysical Journal, 859, 55, doi: [10.3847/1538-4357/aabf95](https://doi.org/10.3847/1538-4357/aabf95)
- Despali, G., Giocoli, C., Angulo, R. E., et al. 2016, MNRAS, 456, 2486, doi: [10.1093/mnras/stv2842](https://doi.org/10.1093/mnras/stv2842)

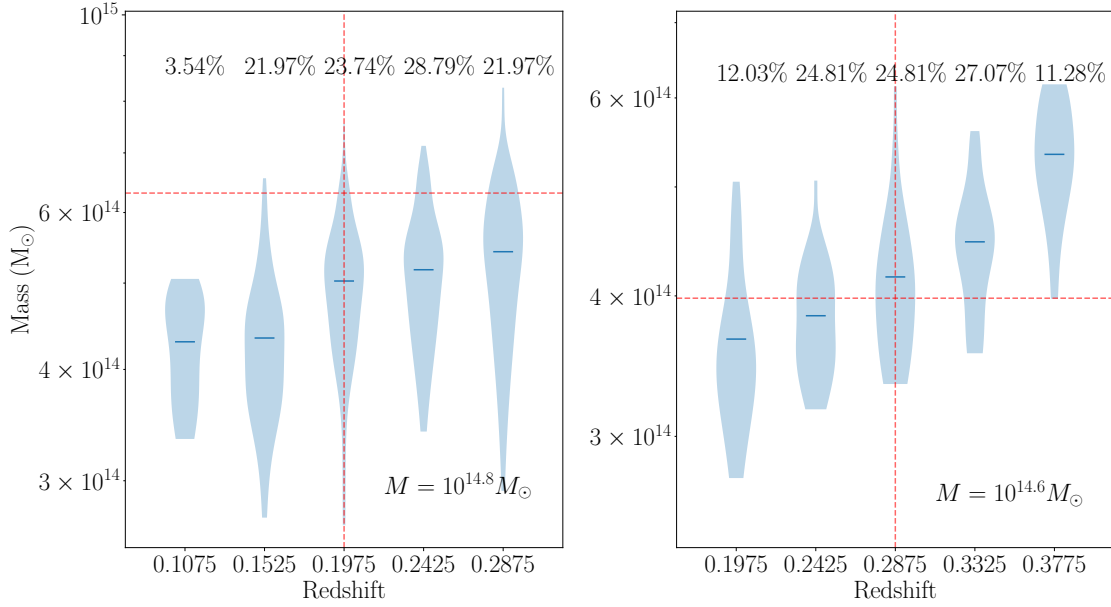


Figure 14. Violin plot for reconstruction of halo with mass $M = 10^{14.8} M_{\odot}$ at $z = 0.1975$ with $ra = 4440''$ and $dec = 5520''$ and another halo which has mass $M = 10^{14.6} M_{\odot}$ at $z = 0.2875$ with $ra = -4440''$ and $dec = -4440''$. The red dashed curve represents the correct redshift and mass estimation. The percentage above one probability distribution represents the percent of total correct estimation corresponding to the respective redshift. The true detection probability was 79.2% and 26.6% respectively.

Eddington, A. S. 1913, Monthly Notices of the Royal Astronomical Society, 73, 359, doi: [10.1093/mnras/73.5.359](https://doi.org/10.1093/mnras/73.5.359)

Hamana, T., Shirasaki, M., & Lin, Y.-T. 2020, PASJ, 72, 78, doi: [10.1093/pasj/psaa068](https://doi.org/10.1093/pasj/psaa068)

Hu, W., & Keeton, C. R. 2002, Physical Review D, 66, doi: [10.1103/physrevd.66.063506](https://doi.org/10.1103/physrevd.66.063506)

Ivezić, Ž., Kahn, S. M., Tyson, J. A., et al. 2019, ApJ, 873, 111, doi: [10.3847/1538-4357/ab042c](https://doi.org/10.3847/1538-4357/ab042c)

Jing, Y. P., & Suto, Y. 2000, ApJ, 529, L69, doi: [10.1086/312463](https://doi.org/10.1086/312463)

—. 2002, The Astrophysical Journal, 574, 538, doi: [10.1086/341065](https://doi.org/10.1086/341065)

Kaiser, N., & Squires, G. 1993, ApJ, 404, 441, doi: [10.1086/172297](https://doi.org/10.1086/172297)

Keeton, C. R. 2001, A Catalog of Mass Models for Gravitational Lensing, arXiv, doi: [10.48550/ARXIV.ASTRO-PH/0102341](https://doi.org/10.48550/ARXIV.ASTRO-PH/0102341). <https://arxiv.org/abs/astro-ph/0102341>

Kelly, B. C. 2007, Astrophys. J., 665, 1489, doi: [10.1086/519947](https://doi.org/10.1086/519947)

Krause, E., & Hirata, C. M. 2010, A&A, 523, A28, doi: [10.1051/0004-6361/200913524](https://doi.org/10.1051/0004-6361/200913524)

Laureijs, R., Amiaux, J., Arduini, S., et al. 2011, Euclid Definition Study Report, arXiv, doi: [10.48550/ARXIV.1110.3193](https://doi.org/10.48550/ARXIV.1110.3193). <https://arxiv.org/abs/1110.3193>

Leonard, A., Lanusse, F., & Starck, J.-L. 2014, MNRAS, 440, 1281, doi: [10.1093/mnras/stu273](https://doi.org/10.1093/mnras/stu273)

Li, X., & Mandelbaum, R. 2022, arXiv e-prints, arXiv:2208.10522. <https://arxiv.org/abs/2208.10522>

Li, X., Yoshida, N., Oguri, M., Ikeda, S., & Luo, W. 2021, ApJ, 916, 67, doi: [10.3847/1538-4357/ac0625](https://doi.org/10.3847/1538-4357/ac0625)

Li, X., Miyatake, H., Luo, W., et al. 2022, PASJ, 74, 421, doi: [10.1093/pasj/psac006](https://doi.org/10.1093/pasj/psac006)

Mandelbaum, R., Miyatake, H., Hamana, T., et al. 2017, Publications of the Astronomical Society of Japan, 70, doi: [10.1093/pasj/psx130](https://doi.org/10.1093/pasj/psx130)

Mandelbaum, R., Lanusse, F., Leauthaud, A., et al. 2018a, MNRAS, 481, 3170, doi: [10.1093/mnras/sty2420](https://doi.org/10.1093/mnras/sty2420)

Mandelbaum, R., Miyatake, H., Hamana, T., et al. 2018b, PASJ, 70, S25, doi: [10.1093/pasj/psx130](https://doi.org/10.1093/pasj/psx130)

Massey, R., Rhodes, J., Ellis, R., et al. 2007, at, 445, 286, doi: [10.1038/nature05497](https://doi.org/10.1038/nature05497)

Miyazaki, S., Oguri, M., Hamana, T., et al. 2018, PASJ, 70, S27, doi: [10.1093/pasj/psx120](https://doi.org/10.1093/pasj/psx120)

Moore, B., Ghigna, S., Governato, F., et al. 1999, The Astrophysical Journal, 524, L19, doi: [10.1086/312287](https://doi.org/10.1086/312287)

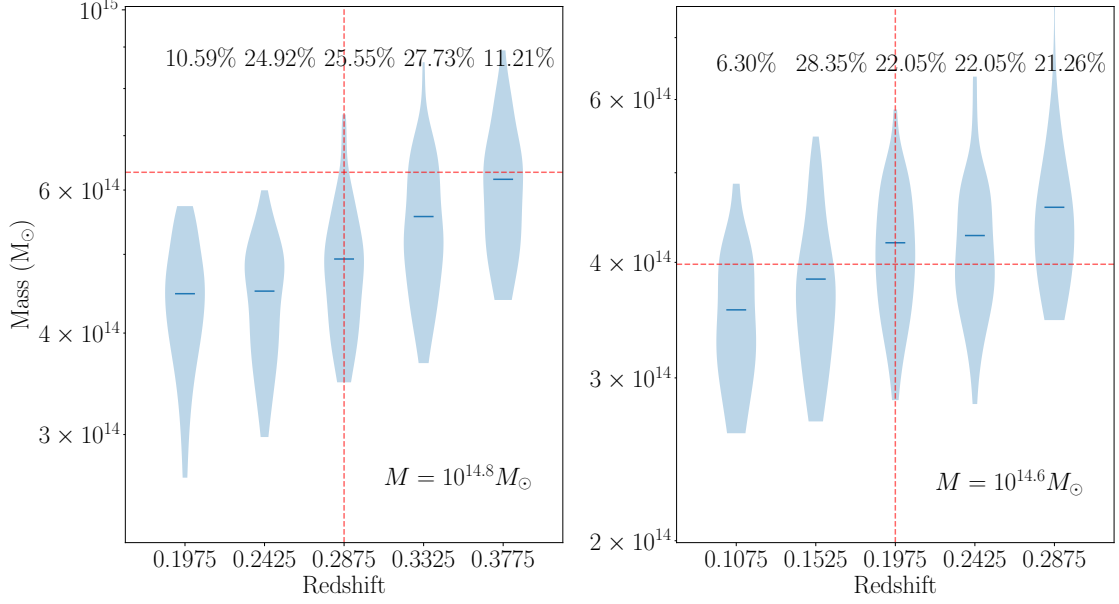


Figure 15. Violin plot for reconstruction of halo with mass $M = 10^{14.8}M_{\odot}$ at $z = 0.2875$ with $ra = 4440''$ and $dec = 5520''$, second halo which has mass $M = 10^{14.6}M_{\odot}$ at $z = 0.1975$ with $ra = 0''$ and $dec = 0''$, and the last halo which has mass $M = 10^{15.2}M_{\odot}$ at $z = 0.3775$ with $ra = -4440''$ and $dec = -4440''$. We adopted dictionaries composing halos of mass $M = 10^{14.6}M_{\odot}$ and $M = 10^{14.8}M_{\odot}$. The red dashed curve represents the correct redshift and mass estimation. The percentage above one probability distribution represents the percent of total correct estimation corresponding to the respective redshift. The true detection probability was 64.2% and 50.8% respectively.

Navarro, J. F., Frenk, C. S., & White, S. D. M. 1997, The Astrophysical Journal, 490, 493, doi: [10.1086/304888](https://doi.org/10.1086/304888)

Navarro, J. F., Ludlow, A., Springel, V., et al. 2010, MNRAS, 402, 21, doi: [10.1111/j.1365-2966.2009.15878.x](https://doi.org/10.1111/j.1365-2966.2009.15878.x)

Oguri, M., Lee, J., & Suto, Y. 2003, The Astrophysical Journal, 599, 7, doi: [10.1086/379223](https://doi.org/10.1086/379223)

Oguri, M., Taruya, A., & Suto, Y. 2001a, The Astrophysical Journal, 559, 572, doi: [10.1086/322513](https://doi.org/10.1086/322513)

—. 2001b, The Astrophysical Journal, 559, 572, doi: [10.1086/322513](https://doi.org/10.1086/322513)

Oguri, M., Miyazaki, S., Li, X., et al. 2021, PASJ, 73, 817, doi: [10.1093/pasj/psab047](https://doi.org/10.1093/pasj/psab047)

Petri, A., Haiman, Z., & May, M. 2017, Phys. Rev. D, 95, 123503, doi: [10.1103/PhysRevD.95.123503](https://doi.org/10.1103/PhysRevD.95.123503)

Planck Collaboration, Aghanim, N., Akrami, Y., et al. 2020, ApJ, 641, A6, doi: [10.1051/0004-6361/201833910](https://doi.org/10.1051/0004-6361/201833910)

Shirasaki, M., Hamana, T., Takada, M., Takahashi, R., & Miyatake, H. 2019, Monthly Notices of the Royal Astronomical Society, 486, 52, doi: [10.1093/mnras/stz791](https://doi.org/10.1093/mnras/stz791)

Takahashi, R., Hamana, T., Shirasaki, M., et al. 2017, The Astrophysical Journal, 850, 24, doi: [10.3847/1538-4357/aa943d](https://doi.org/10.3847/1538-4357/aa943d)

Tinker, J. L., Robertson, B. E., Kravtsov, A. V., et al. 2010, The Astrophysical Journal, 724, 878, doi: [10.1088/0004-637x/724/2/878](https://doi.org/10.1088/0004-637x/724/2/878)

Zou, H. 2006, Journal of the American Statistical Association, 101, 1418, doi: [10.1198/016214506000000735](https://doi.org/10.1198/016214506000000735)

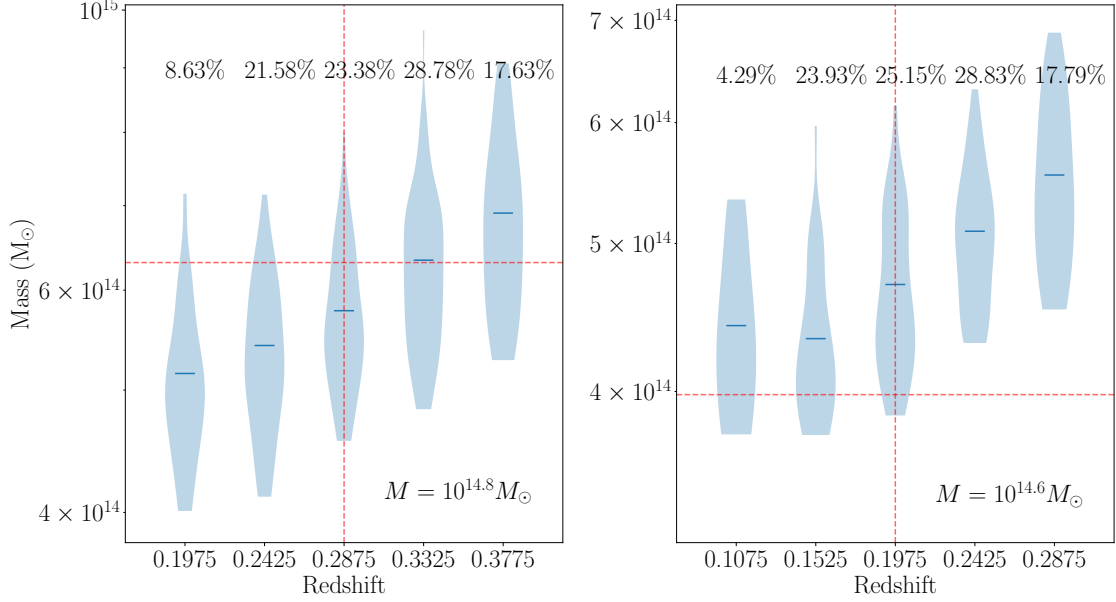


Figure 16. Violin plot for reconstruction of halo with mass $M = 10^{14.8}M_{\odot}$ at $z = 0.2875$ with $ra = 4440''$ and $dec = 5520''$, second halo which has mass $M = 10^{14.6}M_{\odot}$ at $z = 0.1925$ with $ra = 0''$ and $dec = 0''$, and the last halo which has mass $M = 10^{15.2}M_{\odot}$ at $z = 0.3775$ with $ra = -4440''$ and $dec = -4440''$. We adopted dictionaries composing halos of mass $M = 10^{14.6}M_{\odot}$ and $M = 10^{14.8}M_{\odot}$. We first perform a reconstruction with $\lambda = 4$ using dictionary with halo with $M = 10^{15.2}$ and then subtract one realistic reconstruction result. The red dashed curve represents the correct redshift and mass estimation. The percentage above one probability distribution represents the percent of total correct estimation corresponding to the respective redshift. The true detection probability was 62% and 51.2% respectively.

APPENDIX

A. RESULTS WITH $\lambda = 4$

A.1. Mass Estimation

Figs. 17 and 18 show the mass estimation of halos of masses $10^{14.8}$, $10^{15.0}$, $10^{15.2}$ and $10^{15.4} M_{\odot}$, reconstructed using $\lambda = 4$. We observe for the $10^{14.8}M_{\odot}$ halos, while detection at lower redshift with a big λ yields $\lesssim 5\%$ mass estimation bias, the performance of SPLINV decreases drastically as redshift of the halo increases. With a larger λ , we see that the mass estimation for larger mass improves, with performance of reconstructing NFW halos better than that of cuspy NFW halos.

A.2. Redshift Estimation

For redshift estimations, we see a pretty similar result as in Sect. 3.4.3, where the redshift estimation for halo of masses $10^{15.0}$, $10^{15.2}$ and $10^{15.4}$ have consistently less than 5% bias with $z > 0.0625$. However, redshift estimation for halo with mass $10^{14.8}M_{\odot}$ for $z > 0.3325$ shows above 40% mass bias. This is probably due to the fact that, at this redshift level, halo with this mass are hard to detect with $\lambda = 4$, causing we do not have enough data point to correct estimate the mass.

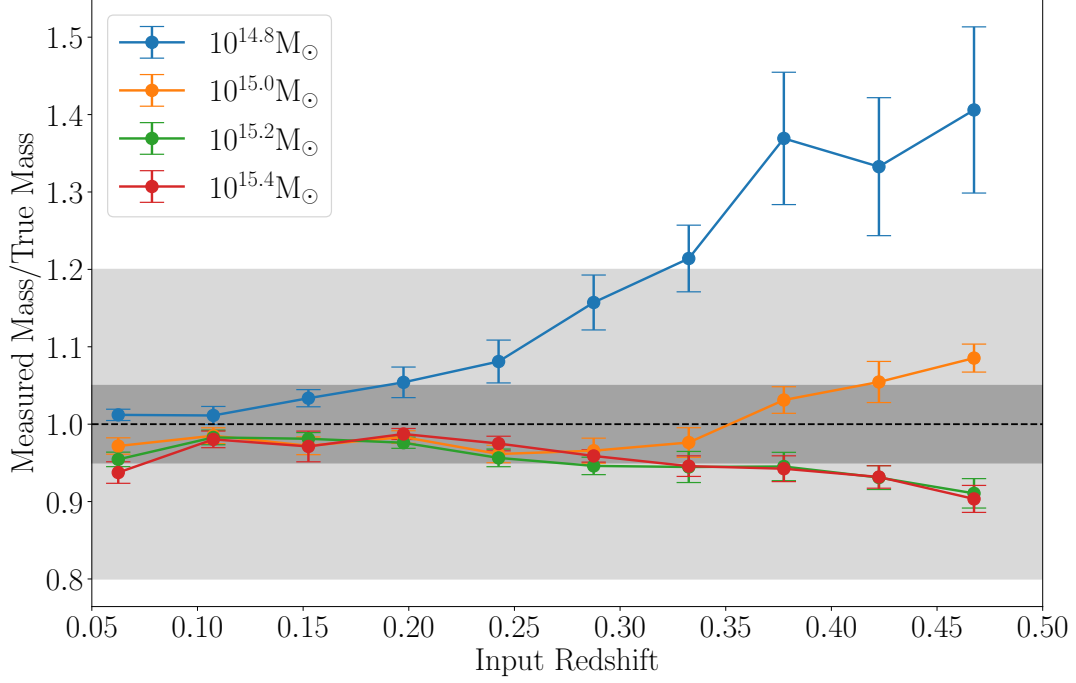


Figure 17. NFW halo Mass Bias for $M = 10^{14.8}, 10^{15.0}, 10^{15.2}$, and $10^{15.4} M_{\odot}$ respectively, reconstructed using $\lambda = 4$. The darker grey area indicate a 5% bias and the lighter grey area indicate a 20% mass bias. The error bar indicate the standard deviation of reconstructed mass with respect to $\frac{m}{c}$ over the range $[0.5, 1]$.

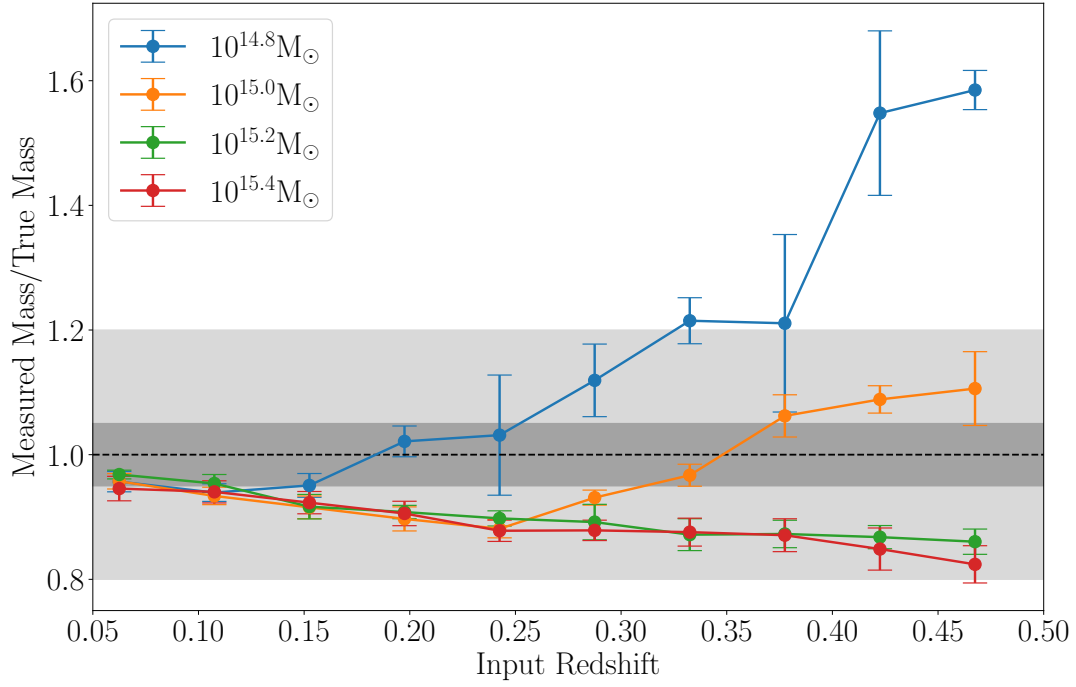


Figure 18. Cuspy NFW halo Mass Bias for $M = 10^{14.8}, 10^{15.0}, 10^{15.2}$, and $10^{15.4} M_{\odot}$ respectively, reconstructed using $\lambda = 4$. The darker grey area indicate a 5% bias and the lighter grey area indicate a 20% mass bias. The error bar indicate the standard deviation of reconstructed mass with respect to $\frac{m}{c}$ over the range $[0.5, 1]$.

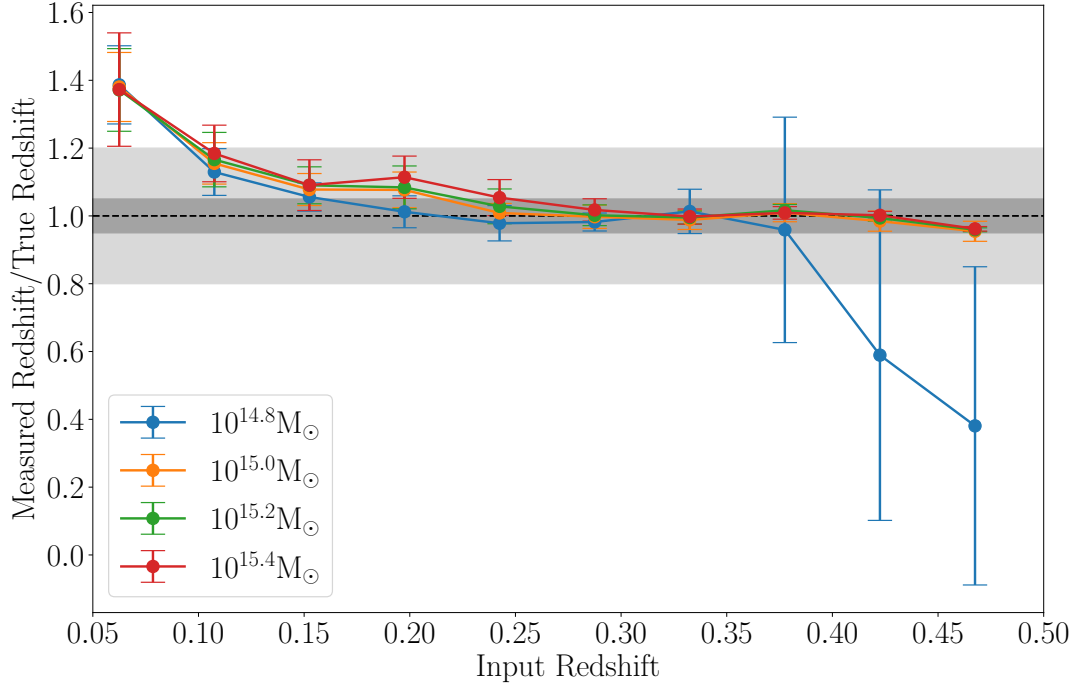


Figure 19. NFW halo Redshift Estimation for $M = 10^{14.8}, 10^{15.0}, 10^{15.2}$ and $10^{15.4} M_{\odot}$ respectively, reconstructed using $\lambda = 2$. The darker grey area indicate a 5% bias and the lighter grey area indicate a 20% mass bias.

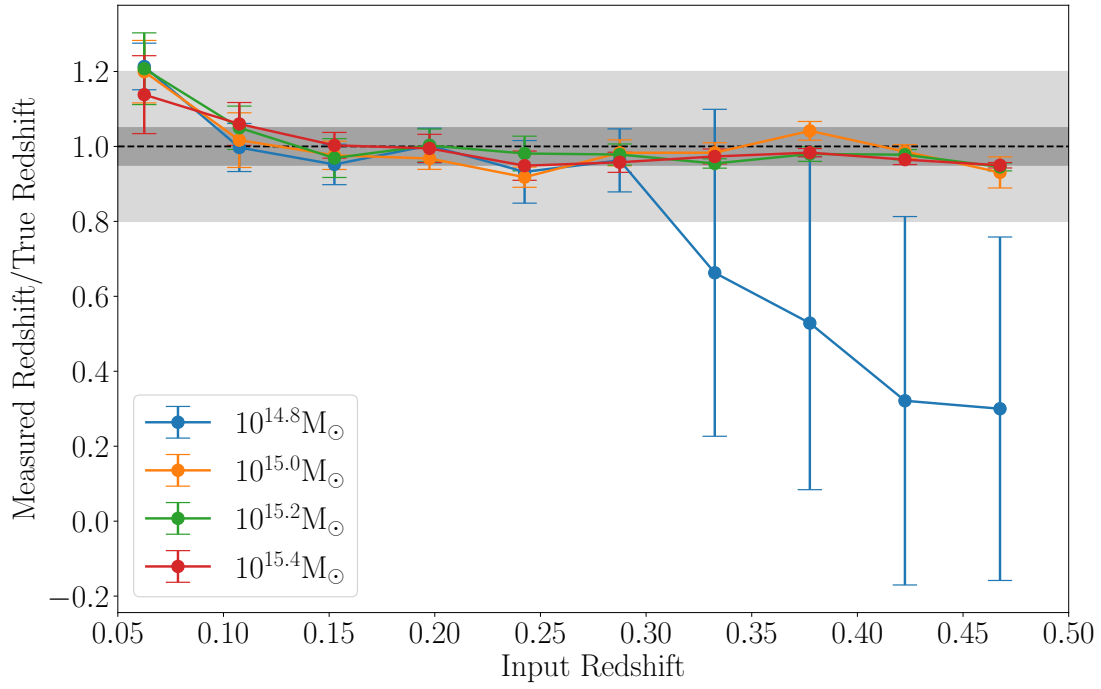


Figure 20. Cuspy NFW halo Redshift Estimation for $M = 10^{14.8}, 10^{15.0}, 10^{15.2}$ and $10^{15.4} M_{\odot}$ respectively, reconstructed using $\lambda = 2$. The darker grey area indicate a 5% bias and the lighter grey area indicate a 20% mass bias.